ACS OMEGA

http://pubs.acs.org/journal/acsodf

Article

Investigating the Role of Classical Ayurveda-Based Incineration Process on the Synthesis of Zinc Oxide Based Jasada Bhasma Nanoparticles and Zn^{2+} Bioavailability

Acharya Balkrishna, Deepika Sharma, Rohit K. Sharma, Kunal Bhattacharya, and Anurag Varshney*

Cite This: *ACS Omega* 2023, 8, 2942−2952

Read Online

ACCESS | Metrics & More | Article Recommendations | Supporting Information

ABSTRACT: Jasada bhasma (JB) is a zinc oxide-based Indian traditional Ayurveda-based herbo-metallic nanoparticle used for the treatment of zinc (Zn) deficiency and autoimmune and inflammatory disorders. JB is made by following the Ayurveda-based guidelines using zinc oxide (ZnO) as a raw material and going through 17 cycles of the high-temperature incineration and trituration process known as "Māraṇa" in the presence of herbal decoctions prepared from the leaves of*Azadirachta indica* and*Aloe vera* gel. These cycles improve the purity of the parent material and transform its physicochemical properties, converting it into nanoparticles. However, there still exists a knowledge gap regarding the role of incineration in the physicochemical transformation of the Zn raw material into JB nanoparticles and the biological interaction of the final product. In the present study, the JB samples obtained during different Māraṇa cycles were carefully studied for their physicochemical transformation using analytical methods such as powdered X-ray diffraction (XRD), small-angle X-ray scattering (SAXS), field emission scanning electron microscopy (FESEM), energy-dispersive X-ray spectroscopy, Fourier transform infrared (FTIR) spectroscopy, Raman spectroscopy, and dynamic light scattering (DLS). According to the XRD results, the Zn and oxygen molecules in hexagonal ZnO wurtzite crystals gradually realigned as a result of repeated heat treatments that caused lattice tension and crystal size reduction from 53.14 to 42.40 nm. A morphological transition from 1.5 μm rod shape to 31 nm in the JB particles can be seen using FESEM and SAXS analyses. The existence of 10 nm-sized nanoparticles in the finished product was confirmed by HRTEM. The presence of ZnO was confirmed in all samples by FTIR and Raman spectroscopies. Cell viability analysis showed an inhibitory concentration 50% of >1000 μg/mL for JB nanoparticles, revealing no adverse effects in human colon Caco-2 cells. A dose-dependent uptake and intracellular accumulation of JB nanoparticles were observed in Caco-2 cells using inductively coupled plasma-based mass spectroscopy (ICP−MS). Bioavailability of Zn^{2+} ions (6% w/w) through JB dissolution in acidic pH 4.0 was observed, representing the stomach and intracellular lysosomal physiological conditions. Therefore, the study showed that the repeated incineration cycles produced biocompatible JB nanoparticles through the physicochemical transformation at molecular levels capable of delivering bioavailable Zn^{2+} ions under physiological conditions. In conclusion, the medicinal properties of JB nanoparticles described in Ayurveda were found to originate from their small size and dissolution properties, formed through the classical incineration-based synthesis process.

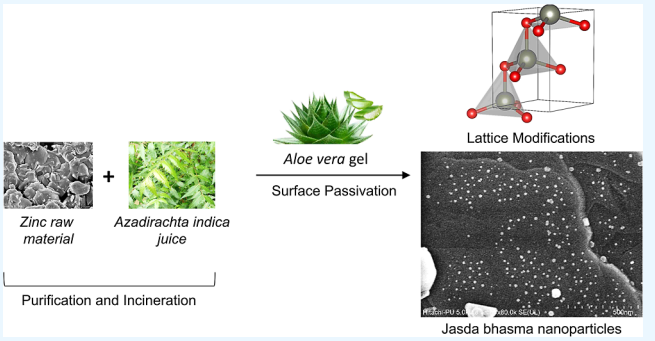

1. INTRODUCTION

The traditional Indian system known as "Ayurveda" existed as far back as 2500 BC.[1,2] Metals in herbo-mineral calyx/ash forms known as "Bhasma" have been applied as stable formulations in Ayurveda with high bioavailability and low-dose therapeutic treatments of various diseases.[1−7] "Jasada bhasma" (JB) is a zinc oxide (ZnO) metal-based herbo-mineral ash composition that is mentioned in the classical texts to attenuate physiological Zn^{2+} deficiency, reduce systemic and localized inflammation, act as an antimicrobial agent, and support wound healing processes.[8,9]

Zinc (Zn) is the second most essential micronutrient after iron required for the preservation of physiological functions. Zn^{2+} ions bind to approximately 2800 proteins as divalent cations and support their catalytic, structural, and regulatory functions.[10] The average amount of Zn in the human body is 2.6 g, and it is distributed in a controlled manner across the body's organs to maintain homeostasis.[10] Since the body does not have a specific location for storing Zn, it needs to be

Received: August 22, 2022
Accepted: December 27, 2022
Published: January 9, 2023

https://doi.org/10.1021/acsomega.2c05391
ACS Omega 2023, 8, 2942−2952

Table 1. Interplanar Distance d_{hkl}, Lattice Parameters a and c, Crystallite Size (D), Microstrain (ε), Dislocation Density (δ), and Bond Length of Zn−O ($L_{(Zn-O)}$).[a]

	planes	(d_{hkl}) Å	(a) Å	(c) Å	(D) nm	(ε) x 10^{-3}	(δ) x 10^{-4} $(nm)^{-2}$	$L_{(Zn-O)}$ Å
	(100)	2.80						
cycle 1	(002)	2.53	3.24	5.06	53.15	2.47	3.54	1.96
	(101)	2.47						
	(100)	2.80						
cycle 4	(002)	2.54	3.23	5.08	50.84	2.51	3.87	1.96
	(101)	2.47						
	(100)	2.86						
cycle 8	(002)	2.53	3.30	5.07	50.95	2.55	3.85	1.98
	(101)	2.46						
	(100)	2.83						
cycle 12	(002)	2.53	3.27	5.06	49.18	2.59	4.13	1.97
	(101)	2.46						
	(100)	2.82						
cycle 16	(002)	2.53	3.26	5.07	45.97	2.84	4.73	1.97
	(101)	2.46						
	(100)	2.80						
cycle 17	(002)	2.54	3.24	5.08	42.40	3.10	5.56	1.96
	(101)	2.47						

[a]Calculation of various parameters for JB cycle 17 as an example reported using powdered XRD analysis presented in the Supporting Information file (Supporting Information S1: the d_{hkl} values were obtained from the XRD instrument for each value of scanning angle (2θ); S2: calculation of lattice constants "a" and "c"; S3: calculation of crystallite size (D) from the Scherrer equation (Equation S5); S4: calculation of microstrain (ε) using equation S6; S5: calculation of dislocation density (δ) using equation S7; and S6: calculation of the bond length of Zn−O $(L_{(Zn-O)})$ using equations S8 and S9).

replenished regularly through oral methods to make up for intestinal and non-intestinal loss. The capture, vesicular storage, and systemic translocation of free Zn ions are carried out by a family of Zn transporter proteins and metallothionines found in the apical region of the enterocytes.[11−14] Low bioavailability, inadequate nutritional supply, and chronic disorders such as celiac disease and inflammatory bowel syndrome can all lead to a loss of Zn homeostasis. Immune system dysfunction, growth retardation, emergence of liver problems, and cognitive deficits can all be caused directly or indirectly by Zn deficiency.[15,16] Zn^{2+} supplementation has been seen to reduce patients' risk of developing metabolic disorders and diseases linked to Zn deficiency. JB acting as a source of Zn^{2+} therapeutic supplement has been proven to support the antibacterial activity, delay the onset of diabetes, and show potential as an anticancer medicine.[17−22]

Physicochemical transformation in calyx/ash and removal of impurities present in the raw material are done through the process of "Bhasmikaran", comprising "Shodhana" and "Māraṇa", leading to the synthesis of "Bhasmas". The process of "Shodhana" uses repeated trituration of the raw material with herbal extracts, cow milk, and uric acid following the classical text of "Ayurveda Sar Sangraha".[23] This is followed by the process of "Māraṇa", involving repeated cycles of high-temperature incineration, grinding, and finally surface passivation using herbal extracts. This transforms the raw material into a granulated oxidized calyx form of the metal nanoparticle.[24−26] According to the ancient literature, the sensory examination of color, taste, rheology, flow, fineness, and chemical qualities including total ash, water-soluble ash, acid-insoluble ash, and loss on drying (LOD) content was used to verify the quality of the synthesized metal bhasmas.[3,26] In the present times, more precise scientific instrumentations are used for conducting qualitative and quantitative analysis of the bhasma nanoparticles.[3,27,28]

In this study, we used advanced analytical techniques such as Fourier transform infrared (FTIR) spectroscopy, powdered X-ray diffraction (XRD), small-angle X-ray scattering (SAXS), field emission scanning electron microscopy (FESEM), Raman spectroscopy, dynamic light scattering (DLS)-based particle size distribution analysis, and energy-dispersive X-ray (EDX) spectroscopy for evaluating the physical and chemical transformation of JB. We evaluated JB samples obtained at various phases of the synthesis process, taking into consideration changes in crystallinity, shape, size, and chemical compositions of materials over different "Māraṇa" process cycles. Furthermore, we investigated the biocompatibility of JB in human colon Caco-2 cells under in vitro conditions. We also quantified the uptake of JB particles in the Caco-2 cells and the amount of free Zn^{2+} ions released from JB through dissolution under physiologically relevant pH conditions.

2. EXPERIMENTAL SECTION

2.1. Reagents. JB samples were obtained from Divya Pharmacy in Haridwar, India. The raw material was triturated (Shodhana) 7 times with herbal decoction and cow milk before beginning the "Māraṇa" procedure according to the ancient book "Ayurveda Sar Sangraha". The purified Zn metal was ground, sieved, and mixed with *Azadirachta indica* leaf juice before being incinerated at ∼400 °C. The "Māraṇa" procedure was used 17 times, with samples taken at various stages of the process. The final 17th incineration cycle samples were obtained following mild-heat treatment in the presence of *Aloe vera* juice. Dulbecco's modified Eagle's medium (DMEM), fetal bovine serum (FBS), antibiotics, and trypsin−EDTA were purchased from Thermo Fisher Scientific (Waltham, MO, USA).

2.2. Powdered X-Ray Diffraction. The diffraction patterns for the JB samples were obtained using an X'Pert Pro X-ray powdered diffraction instrument (Malvern Pan-

https://doi.org/10.1021/acsomega.2c05391
ACS Omega 2023, 8, 2942−2952

alytical, Malvern, UK). Cu K-alpha-1 was used as a radiation source with a wavelength of 1.54 Å and operating conditions of 45 kV and 40 mA. For determining the lattice parameters, measurements were taken in the presence of a beta filter made of nickel metal and in the temperature range of 20−80 °C.

XRD has been used to evaluate various parameters such as interplanar distance (d_{hkl}), lattice constants (a, c), average crystallite size (D), microstrain (ε), dislocation density (δ), and bond length between Zn−O using mathematical equations which were given as follows:

First, Bragg's law was used to calculate the interplanar distance as shown in eq 1 where "d_{hkl}" is the distance between planes with Miller indices h, k, and l. "n" is the order of diffraction, "λ" is the wavelength of the X-ray source, and "θ" is the incidence angle.

$$2d_{hkl}\sin\theta = n\lambda \tag{1}$$

Lattice constants or parameters defined in terms of dimension of length or distance between atoms (a and c) were determined for the hexagonal wurtzite structure. In the hexagonal wurtzite structure, the negatively charged bigger anions are arranged in hexagonal close packing and the positively charged small cations occupy half of the tetrahedral voids. Equation 2 depicted the dependence of lattice parameters on lattice spacing "d" and miller indexes h, k, and l.

$$\frac{1}{d_{hkl}^2} = \frac{4}{3}\left(\frac{h^2 + hk + k^2}{a^2}\right) + \frac{l^2}{c^2} \tag{2}$$

With the first-order approximation $n = 1$

$$\sin^2\theta = \frac{\lambda^2}{4a^2}\left[\frac{4}{3}(h^2 + k^2 + hk) + \left(\frac{a}{c}\right)^2 l^2\right] \tag{3}$$

The lattice constants "a" and "c" are calculated for (100) and (002) planes, respectively, using eq 4 and are summarized in Table 1.

$$a = \frac{\lambda}{\sqrt{3}\sin\theta};\quad c = \frac{\lambda}{\sin\theta} \tag{4}$$

The effectiveness of XRD was also explored to study the peak broadening effect as a combined result of crystallite size and lattice strain. The crystallite size (D) of JB samples was calculated using the Debye−Scherrer mathematical formula for the most intense peak at (101) indexing at a diffraction angle (2θ = 36.37) with preferential crystallographic orientation using mathematical eq 5

$$D = \frac{k\lambda}{\beta_{hkl}\cos\theta} \tag{5}$$

In the equation, D represents the average crystallite size, k stands for the Scherrer constant (0.89), λ corresponding to the wavelength of the X-ray source (1.54 Å), and β_{hkl} is the full width at half-maxima for the (100) peak which was calculated using Origin pro 19 software (Originlab, Northampton, MA, USA). Similarly, microstrain (ε) or strain-induced broadening as a result of crystal imperfection was calculated using eq 6

$$\epsilon = \frac{\beta_{hkl}}{4\tan\theta} \tag{6}$$

The dislocation density "δ" used to quantify the amount of defect in the crystal was computed using eq 7 and defined as the length of dislocation lines per unit volume of the crystal and summarized in Table 1

$$\delta = \frac{1}{D^2} \tag{7}$$

In addition, the Zn−O bond length in the unit cell was calculated using eq 8.[29]

$$L = \sqrt{\left[\frac{a^2}{3} + \left(\frac{1}{2} - u\right)^2 c^2\right]} \tag{8}$$

In eq 8, "u" corresponds to the positional parameter and determines the amount by which each atom is displaced concerning the adjoining atom along the "c" axis and is calculated using eq 9

$$u = \frac{a^2}{3c^2} + 0.25 \tag{9}$$

The Zn−O bond length for the JB samples at different incineration cycles is listed in Table 1.

2.3. Small-Angle X-ray Scattering. An SAXSpace instrument with an in-line collimation system from Anton Paar, Graz, Austria, equipped with a copper source and a 2D detector were used in the study. SAXS analysis was used to evaluate the structural characteristics of the various dry JB samples by measuring the scattering at extremely small angles ranging from 0.1 to 10° for solid samples. The SAXS analysis provided additional support to XRD in the determination of crystallinity, size, and morphology of the ZnO nanocrystal formed in JB. Generalized Indirect Fourier Transformation (GIFT) software was used to examine the data.[30] Scattering analysis was studied in terms of intensity and scattering vector (q), and morphology analysis was studied by a pair distance distribution function (PDDF).

2.4. FESEM and EDX Spectroscopy. The SU810 FESEM (Hitachi, Japan) was used to investigate the morphology and size of all processed JB samples. Before analysis, the samples' solid powder was drop-casted on stubs surface-coated with carbon tape. Later, a gold−palladium coating was applied to the sample to make it conductible using an MC1000 ion sputter (Hitachi, Japan) at 15 mA for 30 s. SEM images were acquired at 5 and 15 kV voltage levels, with magnification ranging from 22,000x to 1,20,000x. All samples were analyzed for elemental composition using a Brucker X Flash 6130 EDX equipment (Billerica, MA, USA) coupled to the FESEM.

2.5. FTIR and Raman Spectroscopies. The functional groups of JB were analyzed using a Spectrum RX-I Fourier transform infrared spectrophotometer (PerkinElmer, Waltham, MA, USA). An Alpha 300 RA Raman Spectrometer (WITec, Germany) was used to conduct Raman analysis on the dried JB particles. Spectra were collected with a CCD camera connected to a UHT300 spectrometer and a Zeiss 100x (NA = 0.9) lens. The samples were illuminated using a diode laser (532 nm). WITec Project Plus software was used to analyze the Raman spectra.

2.6. Particle Size Distribution Analysis. The hydrodynamic diameter (d, nm) of the JB samples was evaluated using the dynamic light scattering method on a Zetasizer Nano ZS device (Malvern Panalytical, UK). For the analysis, a few drops of ethanol were added to 1 g of JB samples, which were then disseminated in 5% BSA solution and examined in a disposable cuvette.

https://doi.org/10.1021/acsomega.2c05391
ACS Omega 2023, 8, 2942−2952

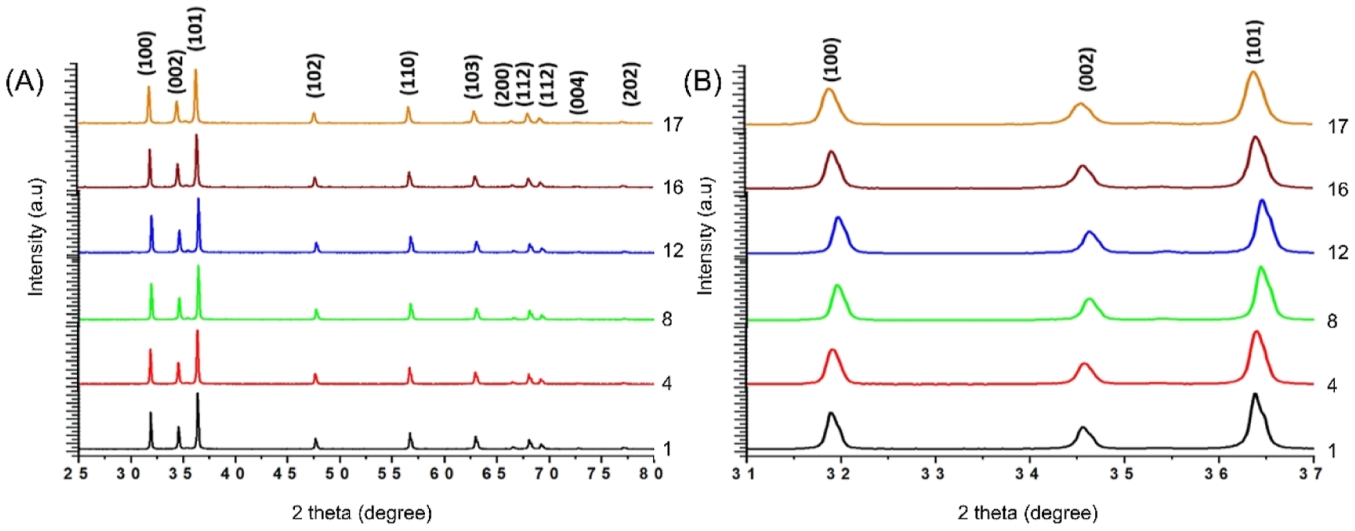

Figure 1. (A) XRD patterns of JB at different cycles of incineration in the angular range of 2θ value from 30 to 80° and (**B**) zoom-in XRD patterns to depict the peak broadening effect at different cycles of incineration.

2.7. Caco-2 Cell Culture. Caco-2 cells were obtained from the National Centre for Cell Science, Pune, India (a local repository for ATCC, USA), and grown in high-glucose DMEM supplemented with 10% heat-inactivated fetal bovine serum (FBS), 10 mM HEPES buffer, 100 IU/mL penicillin, 100 μg/mL streptomycin, and 1% non-essential amino acids. For the cell viability analysis, the Caco-2 cells were plated on a 96-well plate at a seeding density of 1×10^4 cells/well. For uptake study, 2×10^6 cells/well were plated in six-well plates. The cells were pre-incubated overnight before initiating the treatment.

2.8. Cell Viability Analysis. The JB cycle 17 nanoparticles were suspended in 2% FBS containing DMEM at concentrations 1, 3, 10, 30, 100, 300, and 1000 μg/mL. Following pre-incubation, Caco-2 cells were treated with different concentrations of JB cycle 17 nanoparticles and incubated for 24 h. At the end of treatment time, the treatment medium was removed, and the cells were washed with sterile PBS. The cells were incubated for 3 h with a 10 μg/mL concentration of Alamar blue, and fluorescence was measured at Ex. 560 nm/Em. 580 nm using an Envision multimode plate reader (PerkinElmer, Waltham, MA, USA). All the experiments were performed thrice in triplicates, and the results were presented as % cell viability.

2.9. Caco-2 Cell-Based JB Cycle 17 Uptake Study. Caco-2 cells were incubated with JB cycle 17 nanoparticles at concentrations 1, 3, 10, 30, 100, and 300 μg/mL suspended in 2% FBS containing DMEM for a period of 24 h. Following the completion of treatment time, the cells were thoroughly washed with sterile PBS. The cells were then further washed with 0.05% trypsin−EDTA to remove membrane-bound JB nanoparticles. The cells were then treated with 500 μL of RIPA buffer and placed at 4 °C overnight. Next day, the suspension was evenly mixed using a micropipette, and 20 μL of the suspension was used for protein estimation using the Pierce BCA protein assay kit (Thermo Fisher Scientific Waltham, MO, USA) following manufacturer's instructions. The rest of the sample was digested using metal-free concentrated nitric acid and resuspended in metal-free Milli-Q H_2O. The samples were analyzed for a total Zn concentration using ICP−MS (Model: iCAP RQ, Thermo Fisher Scientific, MO, USA). The quantity of Zn was normalized against the protein content per sample tested.

2.10. pH-Based Dissolution of JB Cycle 17 Analysis. A fresh phosphate-buffered solution was prepared, and pH was adjusted to 2.0, 7.0, and 10.0 using concentrated HCl and NaOH. 100 mg of JB cycle 17 was incubated in 1 mL of pH buffers for 24 h on a thermoshaker set at 37 °C and 300 rpm. Next day, the suspensions were centrifuged at 7000 rpm for 45 min for removing the nanoparticle agglomerates. The supernatant was collected and passed through a Whatman 0.1 μm PVDF syringe filter to remove any residue. A standard curve was prepared using zinc sulfate. Following Sabel et al., 25 μL of standards and samples was added to 950 μL of borate buffer (52.63 mM, pH 9.0). Zincon dye (25 μL) was added to the solution, and absorption was measured at 615 nm using a UV-1800 (Shimadzu, Japan) following 5 min of incubation at 20 °C.

2.11. Statistical Analysis. GraphPad Prism 7 was used for statistical analysis (GraphPad Software, San Diego, CA, USA). The data were presented as mean ± standard deviation (SD). Significance between distinct treatment groups was determined using one-way ANOVA, followed by Dunnett's post hoc analysis. At a p-value of <0.05, the results were deemed statistically significant.

3. RESULTS AND DISCUSSION

Zinc (Zn) is an essential micronutrient that is required by several physiologically relevant proteins for catalytic activity and structural stability. Hence, supplementation of Zn supports overcoming chronic disease conditions evolving directly or indirectly through Zn deficiency.[31−34] Nonetheless, due to the inherent dangers associated with metal toxicity, Zn cannot be consumed in its natural condition and oxidized into non-toxic JB for regulating its physiological release. Synthesis of JB was performed through 17 cycles of the incineration process, and particulate samples were collected during 1, 4, 8, 12, 16, and 17 cycles for the analysis of changes in crystallinity, shape, and size.

The XRD spectra were collected at room temperature throughout a diffraction angle 2θ range of 30−80°. All of the samples showed peaks at (100), (002), (101), (102), (110),

https://doi.org/10.1021/acsomega.2c05391
ACS Omega 2023, 8, 2942−2952

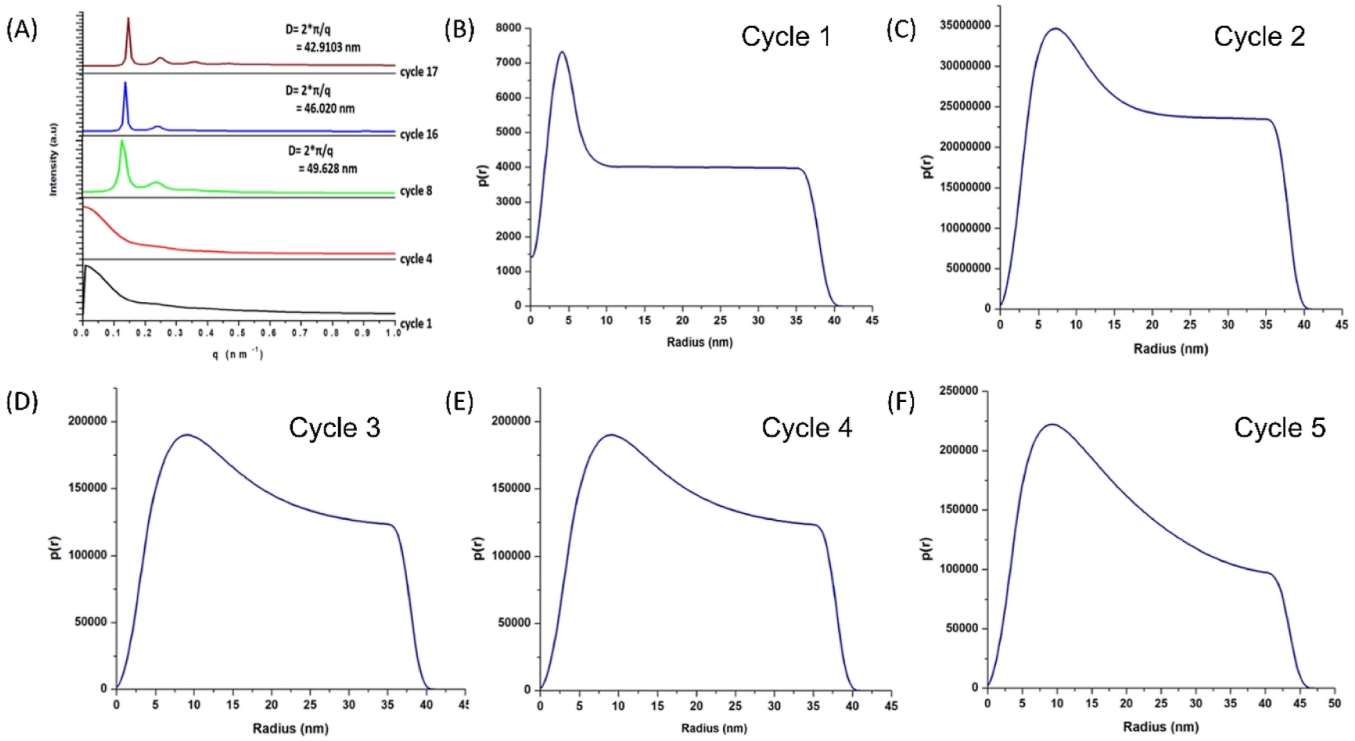

Figure 2. SAXS analysis of JB incineration samples. (**A**) SAXS data for JB samples at different cycles of the incineration process; PDDF obtained from GIFT analysis for (**B**) cycle 1, (**C**) cycle 4, (**D**) cycle 8, (**E**) cycle 16, and (**F**) cycle 17 of incineration.

(103), (200), (112), (201), (004), and (202) indexed at diffraction angles of ∼31.88, 34.55, 36.37, 47.66, 56.70, 62.99, 66.48, 68.06, 69.20, 72.75, and 77.02°, respectively (Figure 1). The interplanar distances were estimated using eq 1 (Table 1). The XRD spectra for JB samples revealed an enriched crystalline nature with intense and sharp peaks representing the interplanar spacing of "d_{hkl}". This spectrum is consistent with ZnO wurtzite crystals generated by high heat and chemical-based flame spray pyrolysis and plasma discharge methods.[35,36] All of the lattice peaks, interplanar distance "d_{hkl}", and lattice constants "a" for all JB samples corresponded well with the XRD peaks of the hexagonal wurtzite structure of pure ZnO with the space group $P6_3mc$ and JCPDS card no. 36-1451 (Table 1, see the example in Supporting Information S1).[37−40] The obtained lattice constant "c" for all JB samples was observed in the range of 5.06−5.08 Å which was lower than that of the standard hexagonal wurtzite structure with the "c" value at 2.21 Å. The lowering of "c" value was a consequence of the presence of iron (Fe) in all samples as observed from EDX (Figure 5C, see the example in Supporting Information S2).[41] Though Fe has affected the lattice parameter but had not altered the overall hexagonal wurtzite structure owing to the comparable size of Fe^{2+} (0.78 Å) with that of Zn^{2+} (0.74 Å) and therefore has easily replaced the Zn^{2+} ion from the lattice. Also, the 2θ value for the (002) plane shifted to a higher value, indicating a lattice disorder (shrinkage) owing to the presence of Fe in the dopant amount.[42,43]

When the XRD spectra from JB incineration cycles 1−17 were compared, a peak broadening effect was seen, which may be attributed to a combined response from crystallite size alteration and increased lattice strain (Figure 1B). The measured crystal sizes of ZnO nanoparticles using Scherer's equation were 53.14 nm (cycle 1), 50.84 nm (cycle 4), 50.94 nm (cycle 8), 49.18 nm (cycle 12), 45.96 nm (cycle 16), and 42.40 nm (cycle 17) (Table 1, see the example in Supporting Information S3). However, because the XRD pattern measures the size of the coherently diffracting domain, the peak broadening observed in the XRD spectra can also represent the shrinkage of nanocrystals as the number of incineration cycles increases. The reducing bond length between Zn−O ($L_{(Zn-O)}$ Å) is represented as 1.98 Å (cycle 8) to 1.95 Å (cycle 17) calculated using eq 8 (Table 1, see the example in Supporting Information S5). On the other hand, the lattice strain ($\varepsilon \times 10^{-3}$) measured in the ZnO nanostructure increases progressively from 2.465 (cycle 1) to 3.101 (cycle 17) (Table 1, see the example in Supporting Information S4). This increased lattice strain correlated with the dislocation density, which measures the number of defects in the samples. It was observed that the dislocation density (δ x 10^{-4} $(nm)^{-2}$) calculated using eq 7 also increased from 3.54×10^{-4} $(nm)^{-2}$ (cycle 1) to 5.56×10^{-4} $(nm)^{-2}$ (cycle 17) (Table 1, see the example in Supporting Information S5).

The aforementioned XRD pattern data demonstrated the progression of the JB samples toward nanosize with a changed crystal structure, followed by the advancement of the incineration process. These variations in the XRD patterns of ZnO nanoparticles correspond closely to those obtained using hydrothermal and co-precipitation techniques, indicating a shift in size and crystal lattice.[44−48] There were no other peaks found in JBs' XRD spectra that might reflect different phases of ZnO or contaminants (Figure 1). Thus, the XRD data suggested that the synthesized JB samples were of high purity.

The JD samples were further investigated using SAXS between 0 and 10° angles. The diffraction pattern exhibited a growing crystalline behavior between cycles 1−8 (Figure 2). This was reflected by the spectral peak broadening between subsequent cycles and transforming into a sharp peak reflecting crystallinity at cycle 8 (Figure 2A). It was observed that the q

https://doi.org/10.1021/acsomega.2c05391
ACS Omega 2023, 8, 2942−2952

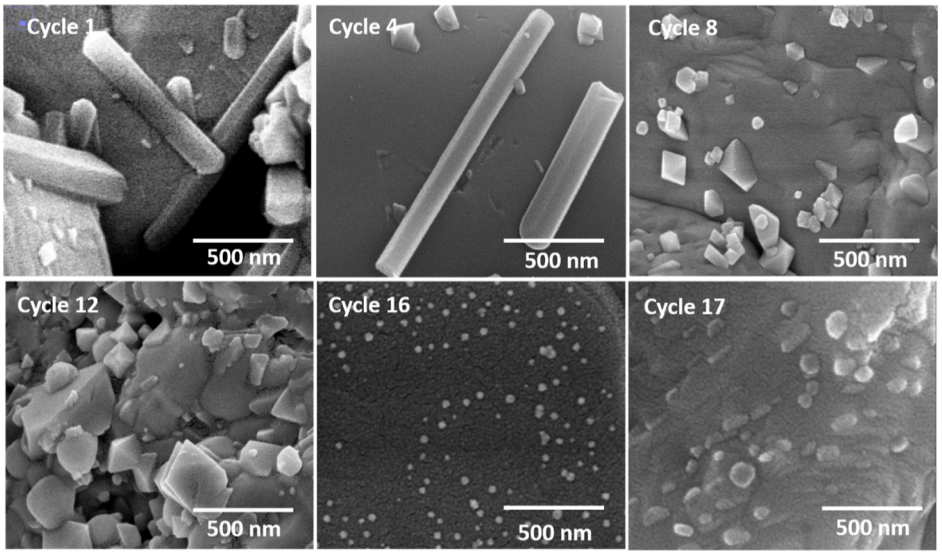

Figure 3. FESEM analysis of JB samples at different cycles of the incineration process.

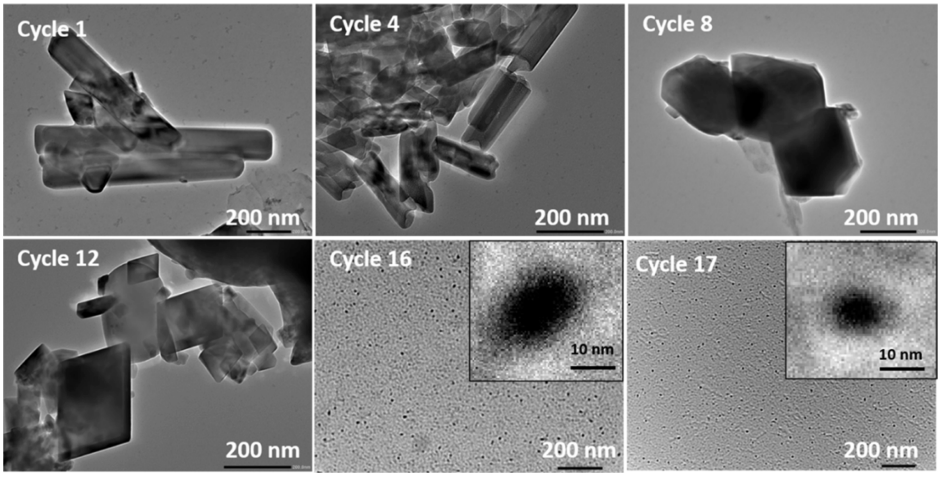

Figure 4. HRTEM analysis of JB samples at different cycles of the incineration process.

value showed a progressive increase from cycle 1 to cycle 17, thus depicting a continuous decrease in size with repeated incineration ($q = 2\pi/D$). The small value of q (broad peak) for the samples at initial incineration cycles 1 and 4 indicated very large particle size, whereas, for the later incineration 8, 16, and 17 cycles, the q values obtained were 0.12658, 0.13649, and 0.14635 and showed smaller particle size corresponding to the interplanar distance (D) equal to 49.6128, 46.0106, and 42.9108 nm, respectively (Figure 2A). The SAXS results validated the XRD analysis results related to the observations made. The sensitivity of SAXS over XRD and DLS is much higher, as it provides better resolution regarding the size and structural changes in the JB particles compared to other analytical methods. In contrast to DLS, which can be utilized for solution samples for monodisperse particles, SAXS can be employed for opaque to solid samples for several types of nanostructures ranging from particles to rod shape and to lamellar.[49] Using generalized inverse Fourier transform (GIFT) analysis for the PDDF, we further investigated the structural change occurring in JB during the incineration cycles.[50] The PDDF obtained for a sample at incineration cycle 1 showed a rod-shaped morphology for JB with a radius of 6.5 nm and a length of 40 nm, which changed to a cylindrical morphology with a radius of 10 nm and a length of 40 nm, throughout incineration cycle 4 (Figure 2B,C). The shape of ZnO eventually altered toward nanoparticles at higher cycles. The form of the PDDF correlated with the particle at higher cycles, 8, 16, and 17 (Gaussian curve). The tailing in the curve might be attributable to the existence of larger size particles, demonstrating the heterogeneous character of the JB precursor particles (Figure 2D−F). In the literature, it has been reported that high-temperature calcination generated ZnO nanoparticles with different morphological forms such as rod shape, nanoflowers, and nanoflakes.[51] Thus, SAXS analysis showed a close correlation between the changes in crystalline structure to the final JB nanoparticle formation progressing with incineration cycles.

The change in size and morphology with incineration progression was studied using FESEM. For the initial cycle between 1 and 4, the results showed large rod-shaped morphologies for the ZnO-based JB particles in the size range of 0.65−1.5 μm (Figure 3).

The observed rod-shaped particle morphology was in good agreement with the SAXS analysis for JB samples obtained between cycles 1 and 4. In ZnO-based JB samples obtained from incineration cycles 8−12, varying heterogenously shaped

https://doi.org/10.1021/acsomega.2c05391
ACS Omega 2023, 8, 2942−2952

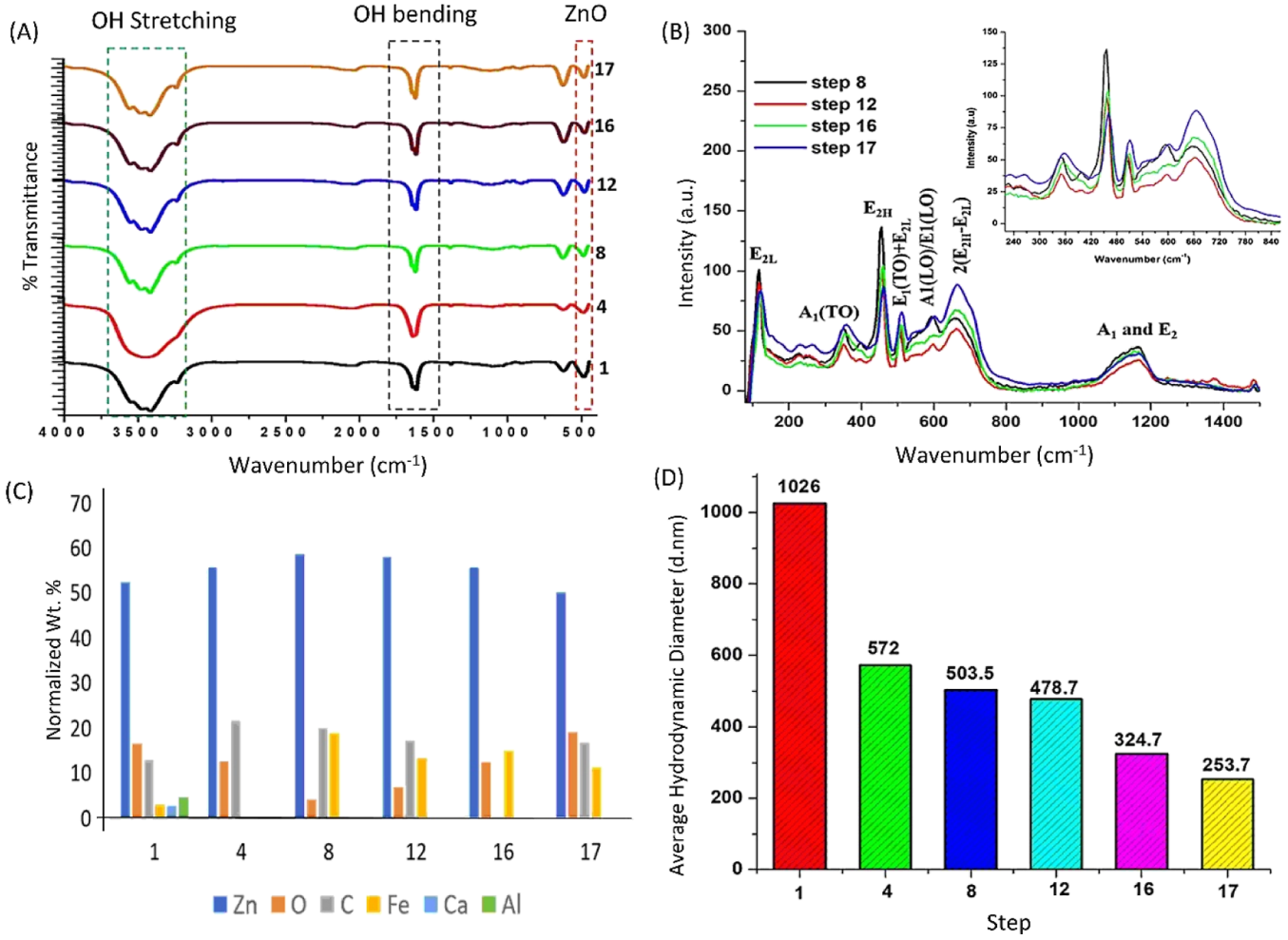

Figure 5. (A) FTIR spectra, (B) Raman spectra, (C) EDX analysis, and (D) DLS measurement of JB at different incineration cycles.

(irregular, triangular, and hexagonal) nanoparticles were observed. The average particle sizes observed were 140 nm (cycle 8) and 70−120 nm (cycle 12). The repeated incineration for final cycles 16 and 17 has enormously reduced the size, and the obtained results depicted the particle morphology with the average size of 17.98 ± 0.51 nm and 31.88 ± 1.17 nm for cycles 16 and 17, respectively (Figure 3). Hence, the results showed a change in the morphology and size distribution of the JB particles changing from micron to nanosize with the transition through the synthesis-associated incineration process. The results also show that the biomedical application of JB in numerous ailments originated from their nanoparticle form, possibly enhancing their bioavailability and cellular uptake.

The morphological investigation of ZnO nanoparticle-based JB at different incineration cycles was also carried out using HRTEM (Figure 4). Similar to FESEM, cycles 1 and 4 depicted a rod-shaped morphology in the micrometer range for ZnO. With progression in incineration cycles, the obtained results showed irregular shapes of ZnO particles in the size range of 200−300 nm. Toward the final incineration cycle, the ZnO-based JB were in particle morphology with an average size of 12.5 and 10 nm for cycles 16 and 17, respectively. The obtained size for the present ZnO nanoparticle-based JB has much more reduced (<50 nm) as compared to that reported in the literature, having the size range of 100 nm to 1 μm.

The numerous functional groups and metal oxide bonds contained in the compounds were analyzed using FTIR in the range of 450−4000 cm^{-1} (Figure 5A). The peaks in the 3200−3500 cm^{-1} range were primarily related to the stretching vibrations of the OH group.[52,53] At all "Māraṇa" cycles, the presence of the OH group can be ascribed to the adsorption of water molecules on the surface of JB samples. Prominent peaks in all JB samples visible in the range of 1600−1650 cm^{-1} were assigned to aromatic C=C bending and C=O from polyphenols, one of the major constituents of *A. indica* and Aloe vera gel used during the synthesis of ZnO nanoparticles (Figure 5A).[54] The metal−oxygen zone was represented by the peak below 800 cm^{-1} (Figure 5A). The presence of the Zn−O stretching mode was confirmed by the occurrence of peaks at 480 cm^{-1} in all samples (Figure 5A).[55] The peak at 620 cm^{-1} corresponded to the Fe−O bending vibration mode and overlapped with the adsorbed H_2O bending peak.[56]

Due to high energy phonons, the Raman spectra showed a highly sharp peak at 451 cm^{-1}, which corresponded to the E_{2H} mode of ZnO (Figure 5B).[22] This wide, asymmetric peak represented the active mode of ZnO in the wurtzite structure. Furthermore, the peaks at 100, 349, and 593 cm^{-1} were likewise based on phonon modes and were denoted as $A_1(TO)$ and $A_1(LO)/E_1(LO)$, respectively (Figure 5B).[57] The remaining peaks at 506 and 661 cm^{-1} were caused by multi-phonon scattering modes and were assigned to the $E_1(TO)$ + E_{2L} and $2(E_{2H}-E_{2L})$ modes, respectively (Figure 5B). The

https://doi.org/10.1021/acsomega.2c05391
ACS Omega 2023, 8, 2942−2952

peak at 1163 cm^{-1} was caused by an acoustic combination of A1 and E2.[58] The spectra of E_{2H} at 451 cm^{-1} were sensitive to internal tension and oxygen mobility. In addition, the polar peak of 593 cm^{-1}, which belonged to Zn interstitial and oxygen vacancy defect complexes, displayed a reversal trend in peak intensity (Figure 5B). This might be attributable to increasing flaws after multiple incineration cycles, and it was also in excellent detected with XRD analyses (Table 1). Furthermore, the signal at 593 cm^{-1} was relatively modest in comparison to the Raman active peak at 451 cm^{-1}, which indicated the high crystallinity and purity of final JB samples obtained by the traditional Ayurveda approach (Figure 5B).

EDX analysis showed the presence of Zn and oxygen (O) along with carbon (C) and iron (Fe) in all the JB particles obtained from different incineration cycles (Figure 5C). The presence of carbon may be attributed to the treatment of bhasma particles with *A. indica* leaf juice and Aloe vera-based decoction during the synthesis process, whereas the presence of Fe in JB can be attributed to the incineration process in the iron pan. Interestingly, the use of herbal decoctions during the "Māraṇa" processes is similar to the current application of herbs for the reduction of metal ions and surface passivation of functional groups during the green synthesis of metal-based nanoparticles.[59,60] Size distribution analysis of JB samples showed an advancing reduction in the particle size distribution of JB samples with progressing incineration cycles (cycle 1: 1026 ± 63 d nm, cycle 4: 572 ± 35.54 d nm, cycle 8: 503.5 ± 38.59 d nm, cycle 12: 478.7 ± 28.96 d nm, cycle 16: 324.7 ± 22.20 d nm, and cycle 17: 253.7 ± 12.06 d nm) (Figure 5D). DLS analysis showed a larger average size of JB nanoparticles compared to XRD and FESEM size analysis. This might be due to the particle agglomeration and settling down of larger particles when suspended in an aqueous medium.[61] Similar to FESEM and HRTEM analysis, the obtained hydrodynamic size was less than the reported size (381 nm).[61]

According to the classical Ayurveda texts, JB is applied as an oral therapeutic supplement for the delivery of Zn ions. In humans, high Zn intakes can induce acute toxicity through induction of nausea, vomiting, diarrhea, headaches, and stomach ache-like symptoms.[62,63] Commercially available Zn nanoparticles applied as food additives and in cosmetics have shown cytotoxicity in Caco-2 and immune cells.[64,65] Hence, due to its nanosize, it is highly important to determine the biocompatibility of JB cycle 17 in Caco-2 cells. Our study showed no induction of cell viability loss in the Caco-2 cell when treated with the JB cycle 17 over a period of 24 h (Figure 6A). The results showed an inhibitory concentration 50% for the JB cycle 17 to be > 1000 μg/mL (Figure 6A). The Recommended Dietary Allowance (RDA) for adults is 8 mg/day for women and 11 mg/day for men.[66] In body, Zn^{2+} homeostasis is maintained mainly by the gastrointestinal barrier cells through modulation of its absorption, secretion, and excretion. Bioavailable Zn ions are mainly absorbed by the small intestine region enterocytes, metabolized and translocated to the systemic circulation reaching the distal organs.[67] Hence, in the present study, we observed a dose-dependent uptake of the JB cycle 17 nanoparticles in the Caco-2 cells following a 24 h treatment (Figure 6B). A significant (p-value <0.001) increase in intracellular uptake of JB cycle 17 was observed at the treatment doses of 100 and 300 μg/mL (Figure 6B). Earlier reports have stated that Zn nanoparticles are taken up by cells through active internalization or endocytosis-free mechanisms leading them to accumulate in

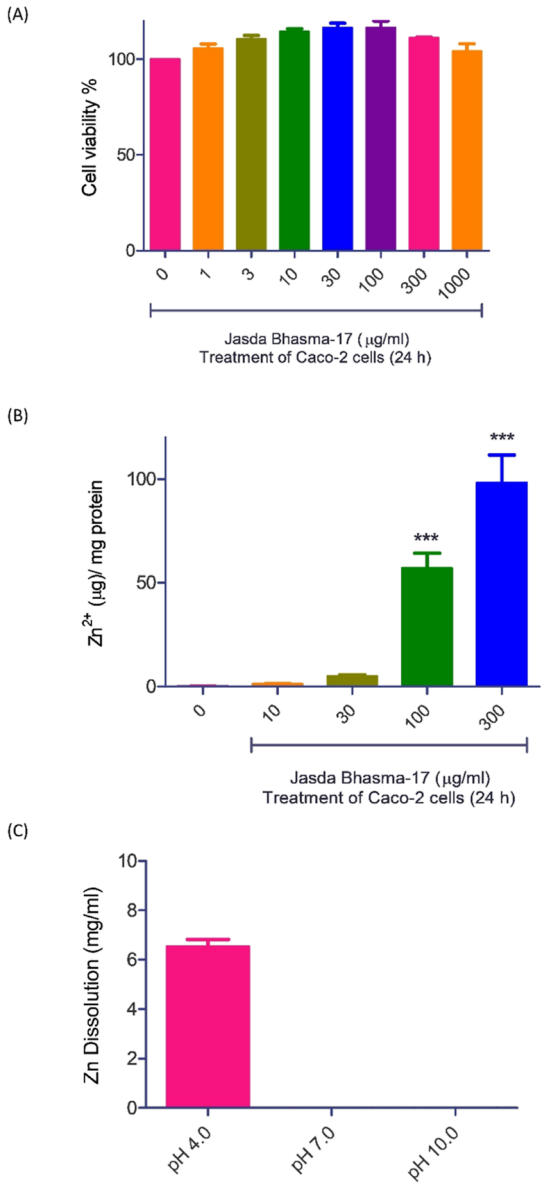

Figure 6. Biological activity of JB cycle 17 in human colon (Caco-2) cells. (**A**) Biocompatibility analysis using the Alamar blue assay, (**B**) Uptake of JB cycle 17 in Caco-2 cells analyzed using ICP−MS and normalized based on the protein content per sample, and (**C**) pH-based acellular dissolution of JB cycle 17 nanoparticles (100 mg/mL) releasing Zn^{2+} ions and detected using Zincon dye. A and C were performed thrice in triplicates. B was performed twice in triplicate. Results are presented as mean ± SD. One-way ANOVA was performed for determining the statistical significance, followed by Tukey's post-hoc analysis. *P*-value of ≥0.05 was considered as statistically significant. In B, *** *p*-value <0.001 (0 μg/mL vs 100 and 300 μg/mL).

the lysosomal region.[68] ZnO nanoparticles have been reported to dissolve at pH between 2.0 and 4.0 that are physiologically present in the stomach region of the gastrointestinal tract and lysosomes.[69,70] Suspension of the JB cycle 17 nanoparticles (100 mg/mL) in PBS buffer set at pH 4.0, 7.0, and 10.0 showed dissolution in acidic conditions [6 mg/mL (6% w/w)] over a period of 24 h (Figure 6C). This showed that under controlled conditions, JB cycle 17 nanoparticles were capable of releasing the bioavailable form of Zn^{2+} ions for intracellular metabolism and release into the systemic circulation similar to

https://doi.org/10.1021/acsomega.2c05391
ACS Omega 2023, 8, 2942−2952

other Zn nanoparticles.[71] In the future studies, we would further explore the cellular mechanism of uptake, metabolism of the final JB samples using in vitro cell models of gastrointestinal tract enterocytes, and their systemic translocation reaching distal organs using in vivo models.

The findings showed that the pre-incineration "Shodhana"-based trituration technique eliminated all impurities from the Zn-based raw material. Progression of the "Māraṇa" cycles continuously changed the size and crystallinity of the raw materials converting them into ZnO nanoparticles. Reduction in the size of JB occurred through the realignment of Zn and oxygen molecules within the Wurtzite crystal causing lattice tension and reduced particle size. The final JB cycle 17 nanoparticles were found to show good biocompatibility and capable of pH-dependent dissolution releasing Zn^{2+} ions for systemic translocation and therapeutics.

4. CONCLUSIONS

In conclusion, the results showed that the repeated incineration cycles induced prompted a major transformation in the crystallinity lattice structure and the morphology of JB converting them into nanoparticles. These classically synthesized JB nanoparticles were found to be highly biocompatible, which were effectively taken up by the intestinal Caco-2 cells. Furthermore, under acidic pH conditions, these JB nanoparticles were found to release free Zn^{2+} ions through dissolution, making them bioavailable for metabolism and systemic translocation. These findings associated with JB are very useful in elucidating the underlying concepts applied in a traditional medicinal system of Ayurveda when using metals as therapeutic agents. In the future, we would further evaluate the biological interaction and systemic translocation of the bioavailable Zn^{2+} released from the JB nanoparticles and their role in modulating complex diseases..

■ ASSOCIATED CONTENT

Supporting Information

The Supporting Information is available free of charge at https://pubs.acs.org/doi/10.1021/acsomega.2c05391.

Calculation of various parameters reported using powdered XRD analysis for JB cycle 17 (PDF)

■ AUTHOR INFORMATION

Corresponding Author

Anurag Varshney − *Drug Discovery and Development Division, Patanjali Research Institute, Haridwar, Uttarakhand 249405, India; Department of Allied and Applied Sciences, University of Patanjali, Haridwar, Uttarakhand 249405, India; Special Centre for Systems Medicine, Jawaharlal Nehru University, New Delhi, Delhi 110067, India;* orcid.org/0000-0001-8509-0882; Email: anurag@patanjali.res.in

Authors

Acharya Balkrishna − *Drug Discovery and Development Division, Patanjali Research Institute, Haridwar, Uttarakhand 249405, India; Department of Allied and Applied Sciences, University of Patanjali, Haridwar, Uttarakhand 249405, India; Patanjali Yog Peeth (UK) Trust, 40 Lambhill Street, Kinning Park, Glasgow G41 1AU, United Kingdom*

Deepika Sharma − *Department of Chemistry & Centre for Advanced Studies in Chemistry, Panjab University, Chandigarh 160014, India*

Rohit K. Sharma − *Department of Chemistry & Centre for Advanced Studies in Chemistry, Panjab University, Chandigarh 160014, India;* orcid.org/0000-0001-8206-1402

Kunal Bhattacharya − *Drug Discovery and Development Division, Patanjali Research Institute, Haridwar, Uttarakhand 249405, India*

Complete contact information is available at: https://pubs.acs.org/10.1021/acsomega.2c05391

Author Contributions

A.B. and A.V. contributed to conceptualization; D.S., R.K.S., and K.B. contributed to methodology; D.S. contributed to validation; D.S., R.K.S., and K.B. contributed to formal analysis; D.S. contributed to investigation; A.B. and A.V. contributed to resources; D.S., R.K.S., and K.B. contributed to data curation; D.S. contributed to writing—original draft; R.K.S., K.B., and A.V. contributed to writing—review and editing; D.S., R.K.S., and K.B. contributed to visualization; R.K.S., K.B., and A.V. contributed to supervision; A.V. contributed to project administration; and A.B. and A.V. contributed to funding acquisition.

Funding

This work has been conducted using research funds from the Patanjali Research Foundation Trust, Haridwar, India.

Notes

The authors declare the following competing financial interest(s): Acharya Balkrishna is a trustee in Divya Yog Mandir Trust, Haridwar, India that governs Divya Pharmacy, Haridwar. In addition, Acharya Balkrishna is one of the founding promoter and holds an honorary managerial position in Patanjali Ayurved Ltd, Haridwar, India. These organizations were not involved in any aspect of this study. Kunal Bhattacharya and Anurag Varshney are employed at Patanjali Research Institute which is governed by Patanjali Research Foundation Trust (PRFT), Haridwar, Uttarakhand, India, a not-for-profit organization. In addition, Anurag Varshney is an Adjunct Professor in Department of Allied and Applied Sciences, University of Patanjali, Haridwar, India; and in Special Centre for Systems Medicine, Jawaharlal Nehru University, New Delhi, India. All other authors declare no competing interests.

■ ACKNOWLEDGMENTS

The authors would like to thank WITec Co. Ltd for Raman spectroscopy and analysis support. We would also like to thank Dr. Seema Gujral, Dr. Nimai Ghosh, and Dr. Pawan Rajput for their technical support in performing the ICP−MS analysis. We are grateful for the prompt administrative assistance provided by Mr. Tarun Rajput, Mr. Gagan Kumar, and Mr. Lalit Mohan.

■ REFERENCES

(1) Jaiswal, Y. S.; Williams, L. L. A glimpse of Ayurveda − The forgotten history and principles of Indian traditional medicine. *Journal of Traditional and Complementary Medicine* **2017**, 7, 50−53.

(2) Galib; Mashru, M.; Patgiri, B.; Barve, M.; Jagtap, C.; Prajapati, P. Therapeutic potentials of metals in ancient India: A review through

Charaka Samhita. *Journal of Ayurveda and Integrative Medicine* **2011**, *2*, 55.
(3) Pal, D.; Sahu, C.; Haldar, A. B. The ancient Indian nanomedicine. *Journal of Advanced Pharmaceutical Technology & Research* **2014**, *5*, 4.
(4) Saleh, T. A. Protocols for synthesis of nanomaterials, polymers, and green materials as adsorbents for water treatment technologies. *Environmental Technology & Innovation* **2021**, *24*, 101821.
(5) Idris, A. M.; Ibrahim, A. E. E.; Abulkibash, A. M.; Saleh, T. A.; Ibrahim, K. E. E. Rapid inexpensive assay method for verapamil by spectrophotometric sequential injection analysis. *Drug Testing and Analysis* **2011**, *3*, 380−386.
(6) Saleh, T. A. Sensing of chlorpheniramine in pharmaceutical applications by sequential injector coupled with potentiometer. *Journal of Pharmaceutical Analysis* **2011**, *1*, 246−250.
(7) Ullah, S.; Khan, S. U.; Saleh, T. A.; Fahad, S. Mad honey: uses, intoxicating/poisoning effects, diagnosis, and treatment. *RSC Adv.* **2018**, *8*, 18635−18646.
(8) Umrani, R.; Paknikar, K. Ayurvedic Medicine Zinc Bhasma: Physicochemical Evaluation, Anti-Diabetic Activity and Safety Assessment. *J. Biomed. Nanotechnol.* **2011**, *7*, 148−149.
(9) Datta, H. S.; Mitra, S. K.; Patwardhan, B. Wound Healing Activity of Topical Application Forms Based on Ayurveda. *Evidence-Based Complementary and Alternative Medicine* **2011**, *2011*, 1−10.
(10) Maares, M.; Haase, H.A Guide to Human Zinc Absorption: General Overview and Recent Advances of In Vitro Intestinal Models. *Nutrients***2020**, *12*(). DOI: 10.3390/nu12030762.
(11) Cragg, R. A.; Christie, G. R.; Phillips, S. R.; Russi, R. M.; Küry, S.; Mathers, J. C.; Taylor, P. M.; Ford, D. A novel zinc-regulated human zinc transporter, hZTL1, is localized to the enterocyte apical membrane. *J. Biol. Chem.* **2002**, *277*, 22789−22797.
(12) Wang, F.; Kim, B. E.; Petris, M. J.; Eide, D. J. The mammalian Zip5 protein is a zinc transporter that localizes to the basolateral surface of polarized cells. *J. Biol. Chem.* **2004**, *279*, 51433−51441.
(13) Cragg, R. A.; Phillips, S. R.; Piper, J. M.; Varma, J. S.; Campbell, F. C.; Mathers, J. C.; Ford, D. Homeostatic regulation of zinc transporters in the human small intestine by dietary zinc supplementation. *Gut* **2005**, *54*, 469−478.
(14) Kim, B. E.; Wang, F.; Dufner-Beattie, J.; Andrews, G. K.; Eide, D. J.; Petris, M. J. Zn2+-stimulated endocytosis of the mZIP4 zinc transporter regulates its location at the plasma membrane. *J. Biol. Chem.* **2004**, *279*, 4523−4530.
(15) Prasad, A. S. Impact of the discovery of human zinc deficiency on health. *J Trace Elem Med Biol* **2014**, *28*, 357−63.
(16) Mohammad, M. K.; Zhou, Z.; Cave, M.; Barve, A.; McClain, C. J. Zinc and liver disease. *Nutr Clin Pract* **2012**, *27*, 8−20.
(17) Medli, S.; Shastry, R.; Sansare, V.; Jadhav, S.; Bansode, H.Investigation of anti-diabetic potential of Jasad bhasma against streptozotocin induced diabetes in rat. *Journal of Pharmacognosy and Phytochemistry***2018**, *7*.
(18) Umrani, R. D.; Paknikar, K. M. Zinc oxide nanoparticles show antidiabetic activity in streptozotocin-induced Type 1 and 2 diabetic rats. *Nanomedicine (Lond)* **2014**, *9*, 89−104.
(19) Babayevska, N.; Przysiecka, L.; Iatsunskyi, I.; Nowaczyk, G.; Jarek, M.; Janiszewska, E.; Jurga, S. ZnO size and shape effect on antibacterial activity and cytotoxicity profile. *Sci. Rep.* **2022**, *12*, 8148.
(20) Metryka, O.; Wasilkowski, D.; Mrozik, A. Evaluation of the Effects of Ag, Cu, ZnO and TiO2 Nanoparticles on the Expression Level of Oxidative Stress-Related Genes and the Activity of Antioxidant Enzymes in Escherichia coli, Bacillus cereus and Staphylococcus epidermidis. *Int. J. Mol. Sci.* **2022**, *23*, 4966.
(21) Khan, F.; Lee, J. W.; Pham, D. N. T.; Khan, M. M.; Park, S. K.; Shin, I. S.; Kim, Y. M. Antibiofilm Action of ZnO, SnO2 and CeO2 Nanoparticles Towards Grampositive Biofilm Forming Pathogenic Bacteria. *Recent Pat. Nanotechnol.* **2020**, *14*, 239−249.
(22) Chandran, S.; Patgiri, B.; Bedarkar, P.; Mathat, D. Anticancer activity of Yashada Bhasma (bioactive nanoparticles of zinc): A human pancreatic cancer cell line study. *AYU (An international quarterly journal of research in Ayurveda)* **2019**, *40*, 58.
(23) Wele, A.; De, S.; Dalvi, M.; Devi, N.; Pandit, V. Nanoparticles of biotite mica as Krishna Vajra Abhraka Bhasma: synthesis and characterization. *Journal of Ayurveda and Integrative Medicine* **2021**, *12*, 269−282.
(24) Patil, S.; Chaudhary, A. K.*Characterization of Yashad Bhasma (Zinc calx) and establishment of the importance of Shodhan (purification)*; Indian Journal of Natural Products, 2021, pp 291−299.
(25) Raghuveer, B.; Jadar, P. G.; Rao, V. N. Analytical Study of Yashada bhasma (Zinc Based Ayurvedic Metallic Preparation) with reference to Ancient and Modern Parameters. *Journal of Allergy & Therapy* **2012**, *S1*, 1−4.
(26) Pareek, A.; Bhatnagar, N. Physico-chemical characterization of traditionally prepared Yashada bhasma. *Journal of Ayurveda and Integrative Medicine* **2020**, *11*, 228−235.
(27) Arya, R. K. Characterization of bio-active nanoparticles - Bhasma an Indian ayurvedic drug. *Indian Journal of Pharmaceutical Education and Research* **2014**, *48*, 61−68.
(28) Kale, B.; Rajurkar, N. Yashad bhasma: Synthesis and characterization. *The Pharma Innovation Journal* **2018**, *7*, 119−122.
(29) Paufler, P. C. S.; Barrett, T. B.*Massalski.Structure of Metals*. 3rd revised edition. Pergamon Press Oxford, New York, Toronto, Sydney, 1980 654 Seiten, 113, vol *16*, p 982,
(30) Ehmann, H. M. A.; Spirk, S.; Doliška, A.; Mohan, T.; Gössler, W.; Ribitsch, V.; Sfiligoj-Smole, M.; Stana-Kleinschek, K. Generalized Indirect Fourier Transformation as a Valuable Tool for the Structural Characterization of Aqueous Nanocrystalline Cellulose Suspensions by Small Angle X-ray Scattering. *Langmuir* **2013**, *29*, 3740−3748.
(31) Roohani, N.; Hurrell, R.; Kelishadi, R.; Schulin, R. Zinc and its importance for human health: An integrative review. *J. Res. Med. Sci.* **2013**, *18*, 144.
(32) Andreini, C.; Banci, L.; Bertini, I.; Rosato, A. Counting the Zinc-Proteins Encoded in the Human Genome. *J. Proteome Res.* **2006**, *5*, 196−201.
(33) Chasapis, C. T.; Loutsidou, A. C.; Spiliopoulou, C. A.; Stefanidou, M. E. Zinc and human health: an update. *Arch. Toxicol.* **2012**, *86*, 521−534.
(34) Ranasinghe, P.; Wathurapatha, W.; Ishara, M.; Jayawardana, R.; Galappatthy, P.; Katulanda, P.; Constantine, G. Effects of Zinc supplementation on serum lipids: a systematic review and meta-analysis. *Nutrition & Metabolism* **2015**, *12*, 26.
(35) Ananth, A.; Dharaneedharan, S.; Seo, H.-J.; Heo, M.-S.; Boo, J.-H. Soft jet plasma-assisted synthesis of Zinc oxide nanomaterials: Morphology controls and antibacterial activity of ZnO. *Chem. Eng. J.* **2017**, *322*, 742−751.
(36) Primc, G.; Brenčič, K.; Mozetič, M.; Gorjanc, M. Recent Advances in the Plasma-Assisted Synthesis of Zinc Oxide Nanoparticles. *Nanomaterials* **2021**, *11*, 1191.
(37) Hall, B. D.; Zanchet, D.; Ugarte, D. Estimating nanoparticle size from diffraction measurements. *J. Appl. Crystallogr.* **2000**, *33*, 1335−1341.
(38) Sahu, S.; Samanta, P. K.; Samanta, P. K. Peak Profile Analysis of X-ray Diffraction Pattern of Zinc Oxide Nanostructure. *Journal of Nano- and Electronic Physics* **2021**, *13*, 05001−1.
(39) Bekru, A. G.; Tufa, L. T.; Zelekew, O. A.; Goddati, M.; Lee, J.; Sabir, F. K. Green Synthesis of a CuO−ZnO Nanocomposite for Efficient Photodegradation of Methylene Blue and Reduction of 4-Nitrophenol. *ACS Omega* **2022**, *7*, 30908−30919.
(40) Gharpure, S.; Yadwade, R.; Ankamwar, B. Non-antimicrobial and Non-anticancer Properties of ZnO Nanoparticles Biosynthesized Using Different Plant Parts of Bixa orellana. *ACS Omega* **2022**, *7*, 1914−1933.
(41) Abdel-Baset, T. A.; Fang, Y.-W.; Anis, B.; Duan, C.-G.; Abdel-Hafiez, M. Structural and Magnetic Properties of Transition-Metal-Doped Zn 1−xFexO. *Nanoscale Res. Lett.* **2016**, *11*, 115.
(42) Pelicano, C. M.; Yanagi, H. Enhanced charge transport in Al-doped ZnO nanotubes designed via simultaneous etching and Al doping of H2O-oxidized ZnO nanorods for solar cell applications. *Journal of Materials Chemistry C* **2019**, *7*, 4653−4661.

https://doi.org/10.1021/acsomega.2c05391
ACS Omega 2023, 8, 2942−2952

(43) Pelicano, C. M.; Raifuku, I.; Ishikawa, Y.; Uraoka, Y.; Yanagi, H. Hierarchical core−shell heterostructure of H2O-oxidized ZnO nanorod@Mg-doped ZnO nanoparticle for solar cell applications. *Materials Advances* **2020**, *1*, 1253−1261.
(44) Koutu, V.; Subohi, O.; Shastri, L.; Malik, M. M. Study the effect of dip in reaction temperature on thermal and electrical properties of ZnO nanoparticles. *Advanced Powder Technology* **2018**, *29*, 2061−2069.
(45) Wasly, H. S.; El-Sadek, M. S. A.; Henini, M. Influence of reaction time and synthesis temperature on the physical properties of ZnO nanoparticles synthesized by the hydrothermal method. *Applied Physics A* **2018**, *124*, 76.
(46) Koutu, V.; Shastri, L.; Malik, M. M. Effect of temperature gradient on zinc oxide nano particles synthesized at low reaction temperatures. *Materials Research Express* **2017**, *4*, 035011.
(47) Faisal, S.; Jan, H.; Shah, S. A.; Shah, S.; Khan, A.; Akbar, M. T.; Rizwan, M.; Jan, F.; Wajidullah; Akhtar, N.; Khattak, A.; Syed, S. Green Synthesis of Zinc Oxide (ZnO) Nanoparticles Using Aqueous Fruit Extracts of Myristica fragrans: Their Characterizations and Biological and Environmental Applications. *ACS Omega* **2021**, *6*, 9709−9722.
(48) Adeel, M.; Saeed, M.; Khan, I.; Muneer, M.; Akram, N. Synthesis and Characterization of Co−ZnO and Evaluation of Its Photocatalytic Activity for Photodegradation of Methyl Orange. *ACS Omega* **2021**, *6*, 1426−1435.
(49) Sakurai, S.*SAXS Evaluation of Size Distribution for Nanoparticles*, 2017. DOI: 10.5772/105981.
(50) Ehmann, H. M. A.; Spirk, S.; Doliška, A.; Mohan, T.; Gössler, W.; Ribitsch, V.; Sfiligoj-Smole, M.; Stana-Kleinschek, K. Generalized Indirect Fourier Transformation as a Valuable Tool for the Structural Characterization of Aqueous Nanocrystalline Cellulose Suspensions by Small Angle X-ray Scattering. *Langmuir* **2013**, *29*, 3740−3748.
(51) Venu Gopal, V. R.; Kamila, S. Effect of temperature on the morphology of ZnO nanoparticles: a comparative study. *Applied Nanoscience* **2017**, *7*, 75−82.
(52) Muhammad, W.; Ullah, N.; Haroon, M.; Abbasi, B. H. Optical, morphological and biological analysis of zinc oxide nanoparticles (ZnO NPs) using *Papaver somniferum* L. *RSC Adv.* **2019**, *9*, 29541−29548.
(53) Frost, R. L.; Ding, Z.; Martens, W. N.; Johnson, T. E.; Kloprogge, J. T. Molecular assembly in synthesised hydrotalcites of formula CuxZn6−xAl2(OH)16(CO3) · 4H2O—a vibrational spectroscopic study. *Spectrochimica Acta Part A: Molecular and Biomolecular Spectroscopy* **2003**, *59*, 321−328.
(54) Handago, D. T.; Zereffa, E. A.; Gonfa, B. A. Effects of Azadirachta Indica Leaf Extract, Capping Agents, on the Synthesis of Pure And Cu Doped ZnO-Nanoparticles: A Green Approach and Microbial Activity. *Open Chemistry* **2019**, *17*, 246−253.
(55) Chen, C.; Yu, B.; Liu, P.; Liu, J.; Wang, L. Investigation of nano-sized ZnO particles fabricated by various synthesis routes. *Journal of Ceramic Processing Research* **2011**, *12*, 420−425.
(56) Ponomar, V.; Adesanya, E.; Ohenoja, K.; Illikainen, M. High-temperature performance of slag-based Fe-rich alkali-activated materials. *Cem. Concr. Res.* **2022**, *161*, 106960.
(57) Damen, T. C.; Porto, S. P. S.; Tell, B. Raman Effect in Zinc Oxide. *Physical Review* **1966**, *142*, 570−574.
(58) Calleja, J. M.; Cardona, M. Resonant Raman scattering in ZnO. *Phys. Rev. B* **1977**, *16*, 3753−3761.
(59) Iqbal, Y.; Raouf Malik, A.; Iqbal, T.; Hammad Aziz, M.; Ahmed, F.; Abolaban, F. A.; Mansoor Ali, S.; Ullah, H. Green synthesis of ZnO and Ag-doped ZnO nanoparticles using Azadirachta indica leaves: Characterization and their potential antibacterial, antidiabetic, and wound-healing activities. *Mater. Lett.* **2021**, *305*, 130671.
(60) Hermandy, M. F. S.; Yusoff, M. Z. M.; Yahya, M. S.; Awal, M. R. The green synthesis of nanoparticle zinc oxide (zno) using aloe vera leaf extract: Structural and optical characterization reviews. *Int J of Emerging Trends in Engineering Res* **2020**, *8*, 6896−6902.
(61) Sharma, C.; Paul, W. Blood compatibility studies of Swarna bhasma (gold bhasma), an Ayurvedic drug. *International Journal of Ayurveda Research* **2011**, *2*, 14.
(62) Wang, B.; Feng, W. Y.; Wang, T. C.; Jia, G.; Wang, M.; Shi, J. W.; Zhang, F.; Zhao, Y. L.; Chai, Z. F. Acute toxicity of nano- and micro-scale zinc powder in healthy adult mice. *Toxicol. Lett.* **2006**, *161*, 115−123.
(63) Porea, T. J.; Belmont, J. W.; Mahoney, D. H., Jr. Zinc-induced anemia and neutropenia in an adolescent. *J Pediatr* **2000**, *136*, 688−690.
(64) Bhattacharya, K.; Kiliç, G.; Costa, P. M.; Fadeel, B. Cytotoxicity screening and cytokine profiling of nineteen nanomaterials enables hazard ranking and grouping based on inflammogenic potential. *Nanotoxicology* **2017**, *11*, 809−826.
(65) Gerloff, K.; Albrecht, C.; Boots, A. W.; Förster, I.; Schins, R. P. F. Cytotoxicity and oxidative DNA damage by nanoparticles in human intestinal Caco-2 cells. *Nanotoxicology* **2009**, *3*, 355−364.
(66) Micronutrients, I. o. M. U. P. o. Dietary Reference Intakes for Vitamin A, Vitamin K, Arsenic, Boron, Chromium, Copper*Iodine, Iron, Manganese, Molybdenum, Nickel, Silicon, Vanadium, and Zinc*; National Academies Press: USA): Washington (DC), USA, 2001.
(67) Krebs, N. F. Overview of zinc absorption and excretion in the human gastrointestinal tract. *J. Nutr.* **2000**, *130*, 1374S−1377S.
(68) Cho, W. S.; Duffin, R.; Howie, S. E.; Scotton, C. J.; Wallace, W. A.; MacNee, W.; Bradley, M.; Megson, I. L.; Donaldson, K. Progressive severe lung injury by zinc oxide nanoparticles; the role of Zn2+ dissolution inside lysosomes. *Part Fibre Toxicol* **2011**, *8*, 27.
(69) Zeng, J.; Shirihai, O. S.; Grinstaff, M. W. Modulating lysosomal pH: a molecular and nanoscale materials design perspective. *J Life Sci (Westlake Village)* **2020**, *2*, 25−37.
(70) Balkrishna, A.; Singh, A.; Singh, J.; Pokhrel, S.; Bhattacharya, K.; Varshney, A. Anti-obesity activity of polyherbal formulation Divya-Medohar-Vati by inhibition of pancreatic lipase activity and triglyceride translocation through enterocytes. *Phytomedicine Plus* **2022**, *2*, 100194.
(71) Liao, C.; Jin, Y.; Li, Y.; Tjong, S. C. Interactions of Zinc Oxide Nanostructures with Mammalian Cells: Cytotoxicity and Photocatalytic Toxicity. *Int. J. Mol. Sci.* **2020**, *21*, 6305.

https://doi.org/10.1021/acsomega.2c05391
ACS Omega 2023, 8, 2942−2952